A satellite-based indicator for diagnosing particulate nitrate sensitivity to precursor emissions: application to East Asia, Europe, and North America

Ruijun Dang[1], Daniel J. Jacob[1], Shixian Zhai[2], Laura Hyesung Yang[1], Drew C. Pendergrass[1], Pierre Coheur[3], Lieven Clarisse[3], Martin Van Damme[3,4], Jin-soo Choi[5], Jin-soo Park[5], Zirui Liu[6], Peifu Xie[7], and Hong Liao[7]

[1] John A. Paulson School of Engineering and Applied Sciences, Harvard University, Cambridge, MA, USA.

[2] Earth and Environmental Sciences Programme and Graduation Division of Earth and Atmospheric Sciences, Faculty of Science, The Chinese University of Hong Kong, Sha Tin, Hong Kong SAR, China.

[3] Université libre de Bruxelles (ULB), Spectroscopy, Quantum Chemistry and Atmospheric Remote Sensing (SQUARES), Brussels, Belgium.

[4] Royal Belgian Institute for Space Aeronomy (BIRA-IASB), Brussels, Belgium.

[5] Air Quality Research Division, National Institute of Environmental Research, Incheon 22689, South Korea.

[6] State Key Laboratory of Atmospheric Environment and Extreme Meteorology, Institute of Atmospheric Physics, Chinese Academy of Sciences, Beijing, China.

[7] Jiangsu Key Laboratory of Atmospheric Environment Monitoring and Pollution Control, Collaborative Innovation Center of Atmospheric Environment and Equipment Technology, School of Environmental Science and Engineering, Nanjing University of Information Science and Technology, Nanjing 210044, China.

Corresponding author: Ruijun Dang (rjdang@g.harvard.edu)

For Table of Contents Only

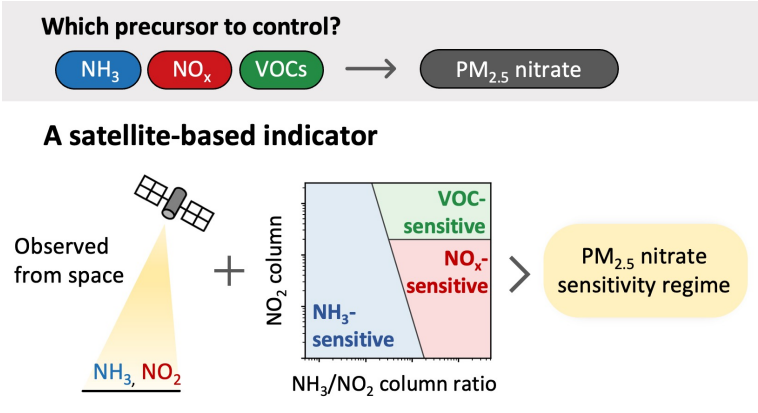

ABSTRACT

Particulate nitrate is a major component of fine particulate matter ($PM_{2.5}$) and a key target for improving air quality. Its formation is varyingly sensitive to emissions of nitrogen oxides ($NO_x \equiv NO + NO_2$), ammonia (NH_3), and volatile organic compounds (VOCs). Diagnosing the dominant sensitivity is critical for effective pollution control. Here we show that satellite observations of the NO_2 column and the NH_3 /NO_2 column ratio can effectively diagnose the dominant sensitivity regimes in polluted regions of East Asia, Europe, and North America, in different seasons. We demarcate the different sensitivity regimes using the GEOS-Chem chemical transport model and apply the method to satellite observations from OMI (NO_2) and IASI (NH_3) in 2017. We find that the dominant sensitivity regimes vary across regions and remain largely consistent across seasons. Sensitivity to NH_3 emissions dominates in the northern North China Plain (NCP), the Yangtze River Delta, South Korea, most of Europe, Los Angeles, and the eastern US. Sensitivity to NO_x emissions dominates in central China, the Po Valley in Italy, the central United States, and the Central Valley in California. Sensitivity to VOC emissions dominates only in the southern NCP in winter. These results agree well with previous local studies. Our satellite-based indicator provides a simple tool for air quality managers to choose emission control strategies for decreasing $PM_{2.5}$ nitrate pollution.

1. INTRODUCTION

Particulate nitrate is a major component of fine particulate matter ($PM_{2.5}$) and often drives $PM_{2.5}$ pollution events in the urbanized world [1-5]. With sulfate and organic fractions of $PM_{2.5}$ decreasing in response to emission controls [6, 7], nitrate has emerged as a key target for further improving air quality [8]. In the eastern United States, wintertime nitrate concentrations exhibited no significant decrease between 2007 and 2015 despite a 36% reduction in NO_x emissions [9]. In eastern China, nitrate levels have remained unresponsive to NO_x emission controls over the past decade [10-12]. New emission control strategies may be needed to manage particulate nitrate to meet $PM_{2.5}$ air quality targets.

Particulate nitrate is produced by the oxidation of nitrogen oxide radicals ($NO_x \equiv NO + NO_2$) to nitric acid (HNO_3), which condenses into the aerosol phase in the presence of alkalinity. We refer to pNO_3^- as the $PM_{2.5}$ component of particulate nitrate, and observations show that it originates mainly from co-condensation with ammonia (NH_3) [10, 13, 14]. The pNO_3^-/HNO_3 thermodynamic equilibrium is highly sensitive to temperature and relative humidity (RH), so that pNO_3^- concentrations are typically highest in winter-spring. The NO_x oxidation process involves hydroxyl radical (OH) and ozone (O_3), both of which

depend on NO_x and volatile organic compounds (VOCs) availability. NO_x, NH_3, and VOCs are thus the three emitted gases serving as precursors for pNO_3^- formation. NO_x in polluted regions is mainly from fuel combustion [15]. NH_3 is from agriculture including fertilization and manure [16], and also has sources from industry [17, 18] and vehicles [19]. VOCs are from combustion, industrial and domestic chemical products, vegetation, and open fires [20]. Understanding which of these three emitted precursors is most important in driving pNO_3^- formation is critical to effective air quality management.

Formation of pNO_3^- is dominantly sensitive to either NH_3 or HNO_3 depending on which is in less supply[21]. This sensitivity can be determined using diagnostic indicators derived from aerosol and gas measurements [22, 23], or with thermodynamic models using these measurements as input [4, 14]. Although a dominant sensitivity to HNO_3 often suggests a corresponding sensitivity to NO_x emissions, the conversion of NO_x to HNO_3 can in fact be limited by VOCs availability under VOC-limited (NO_x-saturated) conditions for O_3 formation, a situation that frequently occurs in urban environments during winter [12, 24]. Other factors further complicate the relationship between pNO_3^- and its precursors, including competing deposition of HNO_3 and pNO_3^- [10, 21], conversion of NO_x to organic nitrates [25], uptake of HNO_3 by alkaline soil dust and sea salt [26], and competition from sulfate for available NH_3 [27]. Chemical transport models (CTMs) can provide a comprehensive description of these processes and serve as a useful tool for diagnosing pNO_3^- sensitivity to emissions through simulations with perturbed emissions [10, 12, 28]. However, this approach is computationally laborious and subject to model errors in particular for emissions.

Satellites measure tropospheric columns of NO_2 (Ω_{NO2}), formaldehyde (Ω_{HCHO}), and NH_3 (Ω_{NH3}). Space-based NO_2 and HCHO measurements started with the GOME instrument in 1995 [29], followed by OMI in 2005 [30] and TROPOMI in 2017 [31], and are now expanding with the geostationary constellation including GEMS over East Asia in 2020 [32], TEMPO over North America in 2023 [33], and the Sentinel-4 satellite over Europe to be launched in 2025 [34]. For NH_3, space-based measurements began with the TES instrument in 2004 [35], followed by IASI in 2007 [36], CrIS in 2012 [37] and soon IRS on Sentinel-4 [38].

In previous work we introduced a new satellite-based method using the $\Omega_{NH3}/\Omega_{NO2}$ ratio to identify the dominant sensitivity of local fine pNO_3^- formation to emissions of NO_x, NH_3, and VOCs under wintertime conditions in East Asia [39]. We demonstrated the method with the GEOS-Chem CTM and then applied it to the satellite observations, evaluating it by comparison with local field and model studies. The approach is similar to the use of the $\Omega_{HCHO}/\Omega_{NO2}$ ratio for diagnosing NO_x- versus VOC-limited conditions for summertime ozone formation [40-42]. Although Ω_{HCHO} is a useful diagnostic of VOC reactivity in summer, we found that Ω_{NO2} was a more useful indicator of VOC-limited conditions for pNO_3^- formation because

of the low Ω_{HCHO} detection capability in winter [43]. Here, we demonstrate the generalization of our satellite-based indicator to other seasons and to Europe and North America, and we use it to identify the seasonality and regionality of pNO_3^- sensitivity regimes.

2. MATERIALS AND METHODS

2.1 GEOS-Chem model

We use the GEOS-Chem CTM (version 13.4.1, DOI: https://zenodo.org/record/6564702) to examine how pNO_3^- formation sensitivity to emissions can be diagnosed from the satellite column observations. The simulations are driven by MERRA-2 meteorology and are conducted at a nested resolution of 0.5° × 0.625° (≈ 50 × 50 km^2) over East Asia (90°–145°E, 10°–55°N), Europe (20°W–40°E, 30°–65°N), and North America (135°–55°W, 15°–60°N), with boundary conditions updated every 3 hours from a 4° × 5° global simulation. We conduct simulations for January, April, July, and October of 2017, and these are viewed in the text as representative of their respective seasons. The 4° × 5° global simulation is spun up for 6 months starting in July 2016 and provides the initial as well as the boundary conditions for the 0.5° × 0.625° continental simulations.

GEOS-Chem includes detailed oxidant-aerosol chemistry [44]. pNO_3^- formation in GEOS-Chem is mainly from thermodynamic equilibrium within the H_2SO_4-HNO_3-HCl-NH_3 system as described by the ISORROPIA II model [45]. Some of the pNO_3^- formation can take place by aerosol uptake and hydrolysis of organic nitrates [46]. GEOS-Chem also includes nitrate formation from uptake by alkaline sea salt [47] and soil dust [48], but these components are mainly in the coarse size range and generally make little contribution to $PM_{2.5}$. Simulation of pNO_3^- is challenging for CTMs because of the complexity and nonlinearity of the processes involved [49, 50], but recent versions of GEOS-Chem show little bias and the ability to capture pNO_3^- variability [10, 39, 51, 52].

Our simulation is the same as previously described in Dang, et al. [39], featuring specific options within the standard GEOS-Chem v.13.4.1. These include the use of Luo's wet deposition scheme to better reproduce pNO_3^- concentrations [51, 52], and the incorporation of aerosol nitrate photolysis which improves simulation of tropospheric NO_2 columns [53]. Anthropogenic emissions are from the global Community Emissions Data System (CEDSv2) inventory [54] superseded by region-specific inventories including MEIC for China [55], KORUSv5 for South Korea [56], and the United States (US) EPA NEI 2016 (https://www.epa.gov/air-emissions-modeling/2016v1-platform). All other emissions are as described in Dang, et al. [53].

Our use of GEOS-Chem for the interpretation of satellite observations in terms of pNO_3^- sensitivity regime relies on the model having a correct representation of pNO_3^- formation processes but not necessarily emissions. Here we evaluate the model's performance in simulating pNO_3^- by comparison to $PM_{2.5}$ surface measurements in 2017 from East Asia, Europe, and the US. East Asian data are collected from previous studies in China [10, 57-66] and from sites managed by South Korea's National Institute of Environmental Research (NIER) and the Acid Deposition Monitoring Network in East Asia (EANET), totaling 22 sites. Site details and pNO_3^- data are provided at XXX (will be uploaded to Harvard Dataverse (open access)). European data are from the European Monitoring and Evaluation Programme network (EMEP, 24 sites) (https://ebas-data.nilu.no/Default.aspx). US data are from the Interagency Monitoring of Protected Visual Environments network (IMPROVE, 147 sites) and the Chemical Speciation Network (CSN, 132 sites) (http://views.cira.colostate.edu/fed/QueryWizard/Default.aspx).

Figure 1 compares observed versus modeled monthly mean surface pNO_3^- concentrations for January, April, July, and October 2017. GEOS-Chem simulates pNO_3^- in East Asia remarkably well across the four seasons. Results In Europe and the US show relatively larger errors, which may reflect the lower concentrations and dynamic range. The model tends to underestimate the high observed pNO_3^- concentrations at sites in the western urban US during winter, probably due to a low bias in winter NH_3 emissions [67].

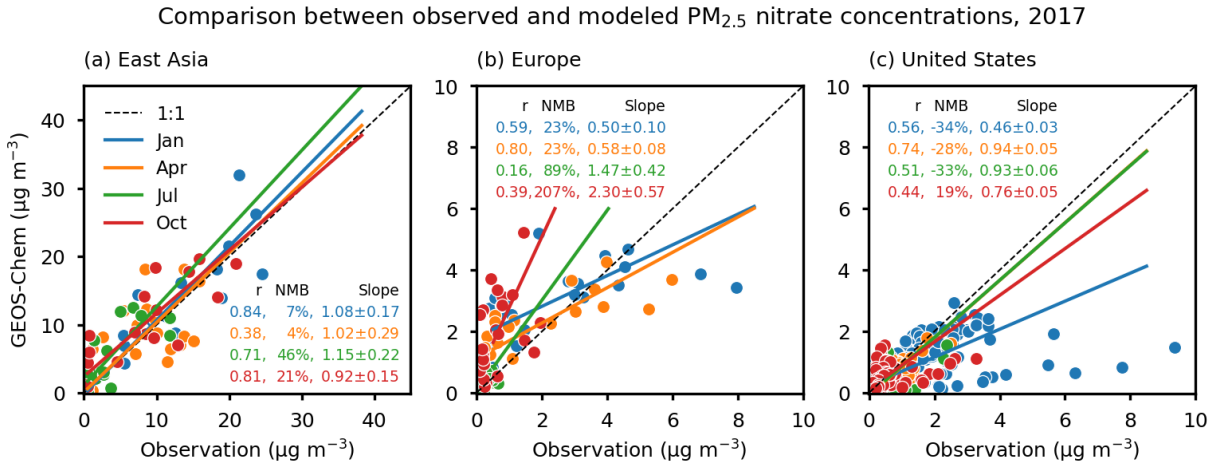

Figure 1: Comparison of observed and modeled monthly mean $PM_{2.5}$ nitrate concentrations at sites in (a) East Asia, (b) Europe, and (c) the United States for January, April, July, and October 2017. Comparison statistics include the correlation coefficient (r), normalized mean bias (NMB), and the reduced-major-axis (RMA) regression line and slope (±95% confidence interval). The 1:1 line is shown as dashed. The panels have different scales.

2.2 Satellite observations of NO_2 and NH_3

We use the same satellite products as in our previous work [39]: version 4 of the NASA OMI NO_2 level 2 product (https://disc.gsfc.nasa.gov/datasets/OMNO2_ 003/summary) and version 3 of the reanalyzed level 2 IASI NH_3 product (https://iasi.aeris-data.fr/catalog/#masthead).

The OMI retrieval measures NO_2 slant columns by fitting the backscattered solar spectrum and converts the data to tropospheric vertical columns [30]. It provides daily coverage at 13:30 local time (LT) with a spatial resolution of 13×24 km^2 at nadir. We filter out pixels with cloud fraction > 0.3, surface reflectance > 0.3, solar zenith angle > 75°, viewing zenith angle > 65°, and those affected by the so-called row anomaly. Pixel observations are gridded and averaged to a resolution of $0.5° \times 0.625°$ to calculate seasonal mean columns. Only grid cells with more than 30 successful retrievals are included in the analysis.

Figure 2 shows the seasonal mean NO_2 columns (Ω_{NO2}) measured by OMI in 2017. We exclude remote areas with winter $\Omega_{NO2} < 2.5 \times 10^{15}$ molec cm^{-2} because diagnosing sensitivity to local emissions in these regions would be inappropriate. OMI observes high NO_2 in densely populated regions such as the East China Plain, the Seoul metropolitan area (SMA) in South Korea, northwestern Europe, northern Italy, California in US, and northeastern US. Ω_{NO2} peaks in winter and is lowest during summer, reflecting the seasonality in photochemical oxidation.

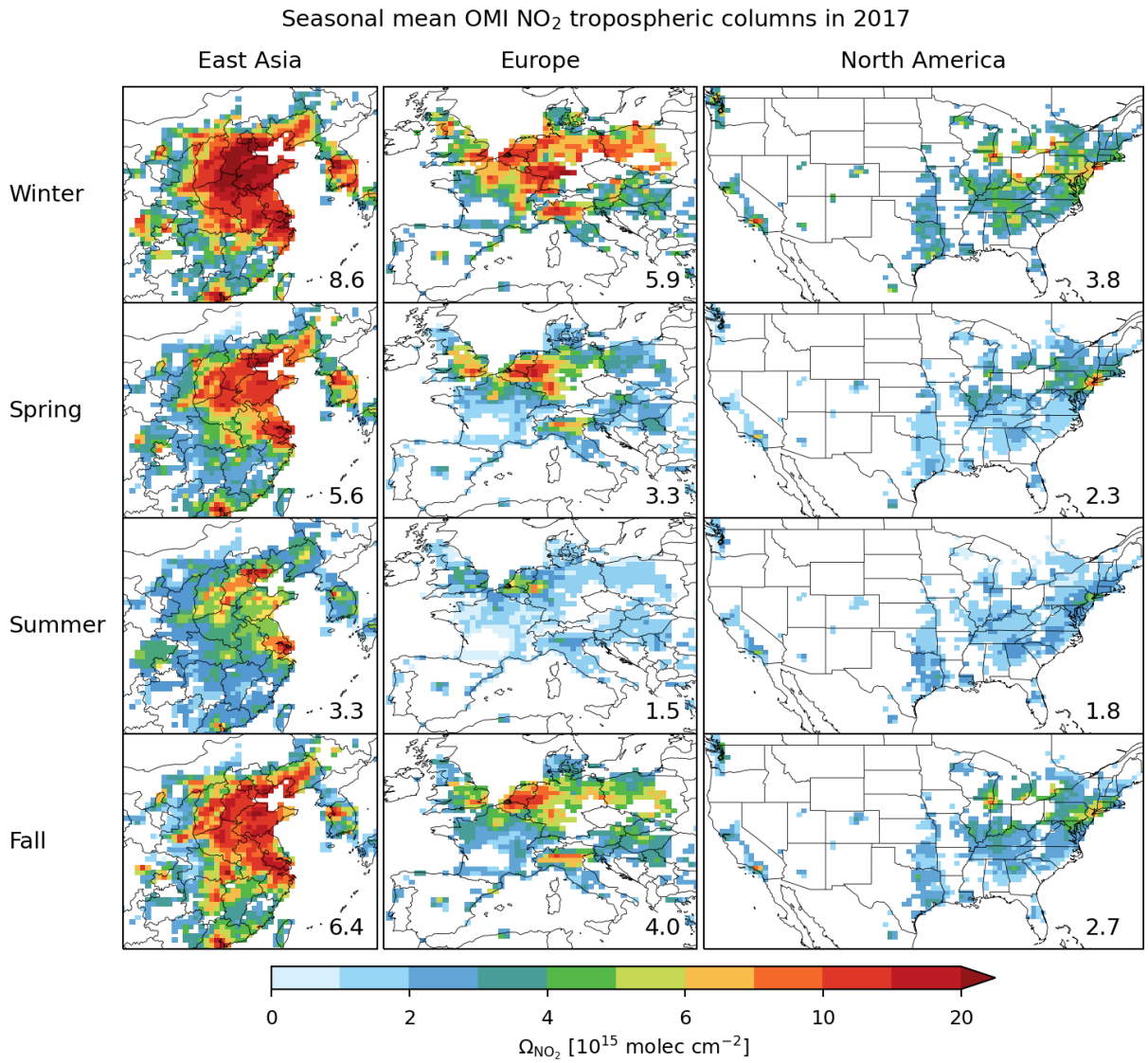

Figure 2: Seasonal mean OMI tropospheric NO_2 columns (Ω_{NO2}) in East Asia, Europe, and North America in 2017. Values are plotted on the 0.5° × 0.625° GEOS-Chem model grid as 3-month averages for winter (DJF), spring (MAM), summer (JJA), and fall (SON). Remote grid cells with winter $\Omega_{NO2} < 2.5 \times 10^{15}$ molec cm^{-2} are excluded. Regional mean values are provided inset, with units of 10^{15} molec cm^{-2}.

The IASI instrument measures atmospheric NH_3 columns using thermal infrared radiation (TIR) emitted by the Earth's surface and atmosphere [68]. It offers global coverage twice daily, at 9:30 LT and 21:30 LT, with a nadir pixel resolution of 12 ×12 km^2. We use only 9:30 LT observations to minimize the time separation with OMI. Only clear-sky observations with cloud fraction < 0.1 are used. The seasonal mean NH_3 columns are calculated using the same method as for OMI NO_2. Further filtering is applied to the gridded wintertime means to remove negative values.

Figure 3 shows the IASI seasonal mean NH_3 columns (Ω_{NH3}) in the polluted regions (as identified in Figure 2) for 2017. High Ω_{NH3} concentrations are observed in agriculturally intensive areas [69]. Peak Ω_{NH3} levels occur in summer, followed by spring, driven by fertilizer application and high temperatures [70]. High temperatures also shift the thermodynamic partitioning of NH_3 towards the gas phase.

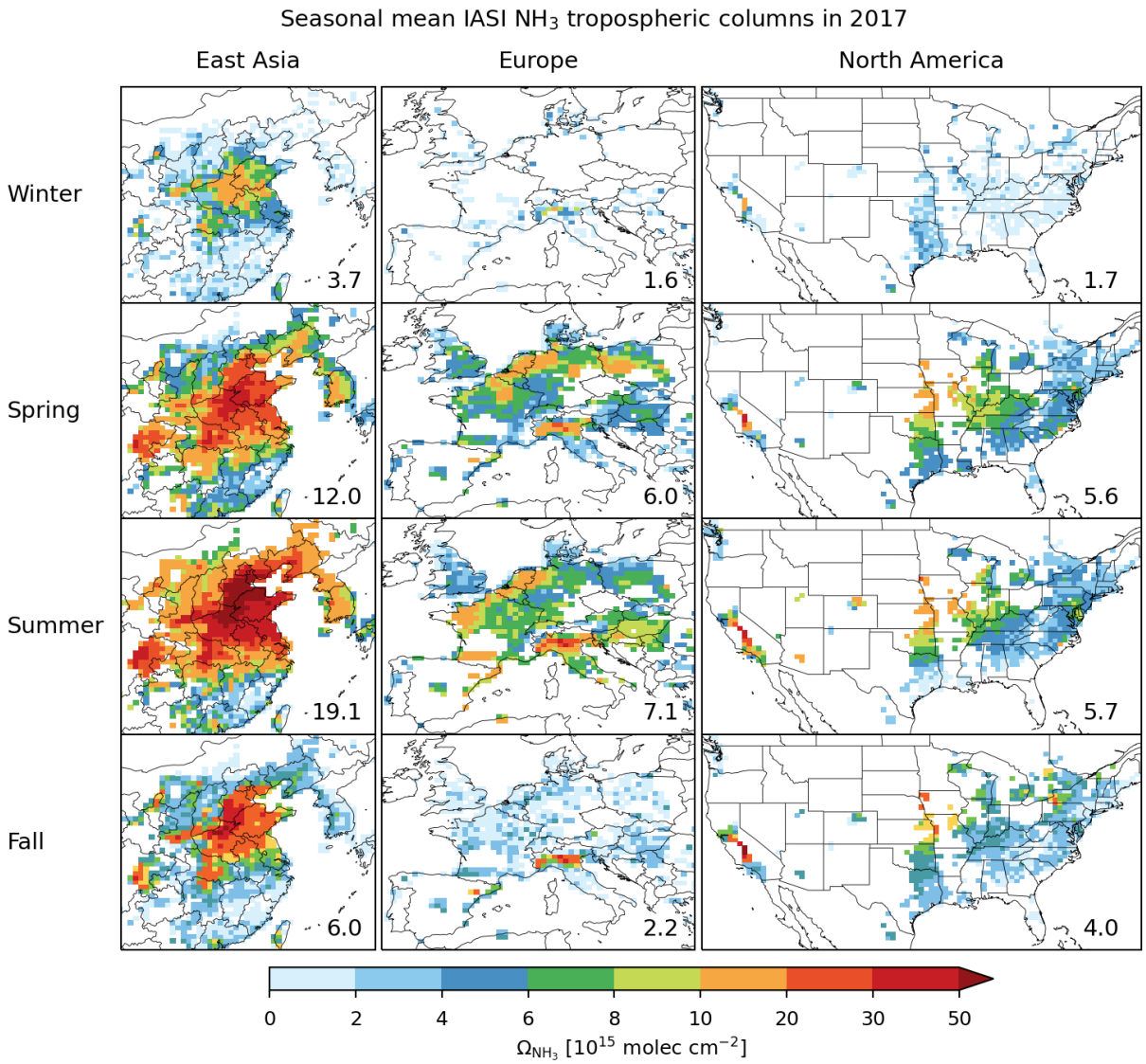

Figure 3: Seasonal mean IASI NH_3 columns (Ω_{NH3}) in East Asia, Europe, and North America in 2017. Values are plotted on the 0.5° × 0.625° GEOS-Chem model grid. White areas indicate either lack of data or remote areas (winter $\Omega_{NO2} < 2.5 \times 10^{15}$ molec cm^{-2} as identified in Figure 2). Regional mean values are provided inset, with units of 10^{15} molec cm^{-2}.

We use the $\Omega_{NH3}/\Omega_{NO2}$ ratio to identify surface pNO_3^- sensitivity. The different seasonalities of Ω_{NO2} and Ω_{NH3} imprint a large seasonality to the $\Omega_{NH3}/\Omega_{NO2}$ ratio (Figure 4). The ratio peaks in summer, with seasonal mean values exceeding 10, and drops to below unity in winter.

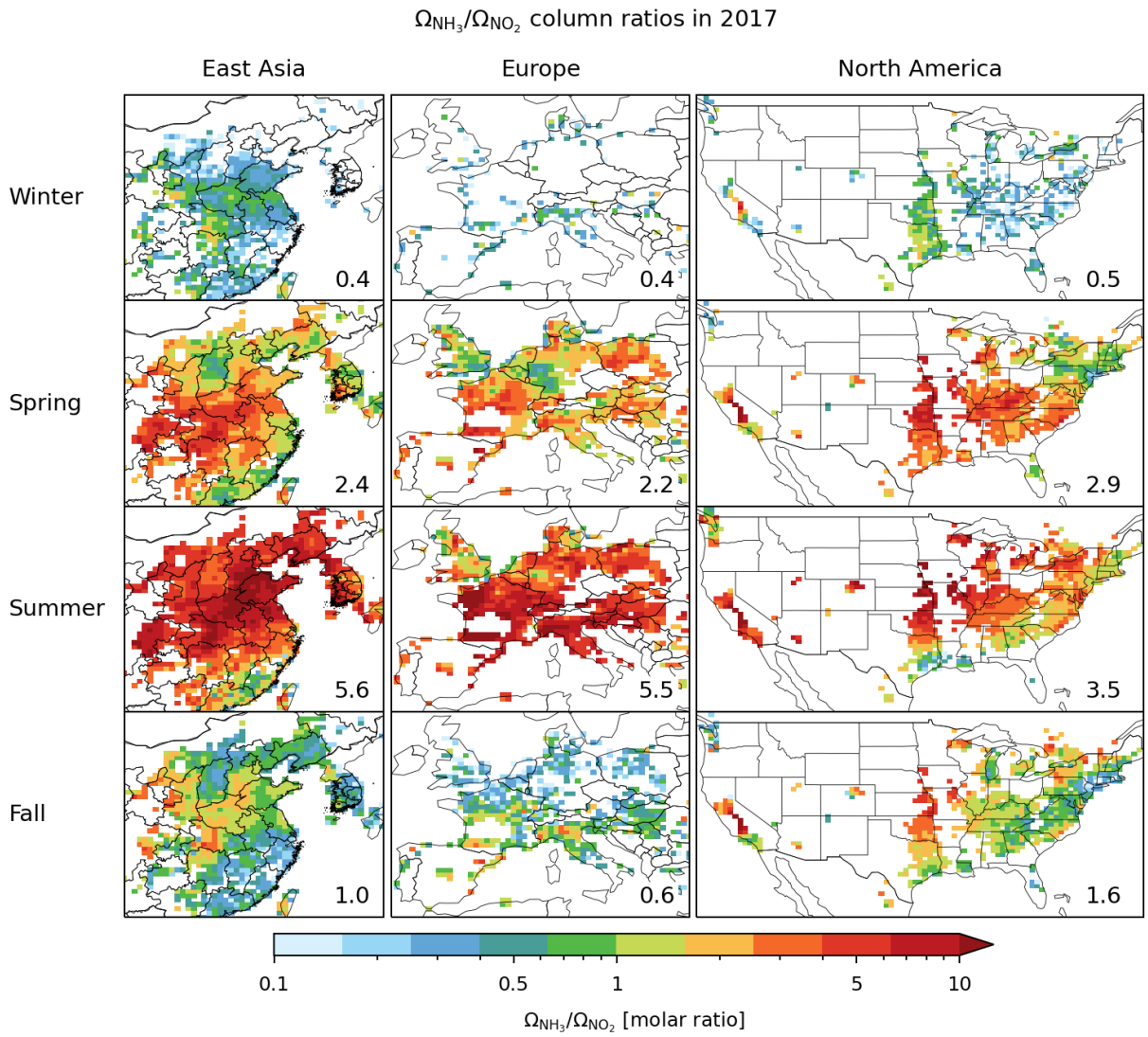

Figure 4: Same as Figure 3 but for columns ratios $\Omega_{NH3}/\Omega_{NO2}$. The seasonal mean column ratios are computed as the ratios of the means.

3. RESULTS AND DISCUSSION

3.1 Particulate nitrate sensitivity regimes in GEOS-Chem

We diagnose the sensitivity of pNO_3^- formation to NO_x, NH_3, and VOCs emissions in GEOS-Chem by conducting sensitivity simulations with 20% reductions in individual precursor emissions. The local

model sensitivity (S_i) of pNO_3^- to the emissions (E_i) of precursor i is calculated from the relative model differences (Δ) between the sensitivity and base simulations as:

$$S_i = \frac{\Delta \log[pNO_3^-]}{\Delta \log E_i} \qquad (1),$$

where [pNO_3^-] refers to monthly mean concentrations in surface air, and i refers to NH_3, NO_x, or VOC. A higher S_i value indicates a greater sensitivity. By comparing sensitivities S_{NOx}, S_{NH3}, and S_{VOC}, we can determine whether pNO_3^- formation in a model grid cell is most NO_x-, NH_3-, or VOC-sensitive.

Previous work by Dang, et al. [39] for wintertime conditions in East Asia found that the dominant sensitivities (NO_x-, NH_3-, or VOC-sensitive) could be separated within a two-dimensional space defined by the column concentration indicator $\Omega_{NH3}/\Omega_{NO2}$ and Ω_{NO2}. The $\Omega_{NH3}/\Omega_{NO2}$ ratio indicates the relative abundance of NH_3 to NO_x, while high Ω_{NO2} diagnoses VOC-limited conditions in the oxidation of NO_x to HNO_3. Figure 5 expands this analysis to other seasons and regions, where the circles represent the dominant sensitivities of pNO_3^- formation for individual 0.5° × 0.625° grid cells in polluted regions (as defined in Figure 2). The column indicator is sampled in GEOS-Chem at the OMI overpass time of 13-14 local time (LT) for NO_2 and at the IASI overpass time of 9-10 LT for NH_3, to emulate satellite observations. Averaging kernels are applied to the model NO_2 vertical profiles following Cooper, et al. [71], to emulate tropospheric NO_2 columns from version 4 of the NASA OMI NO_2 level 2 product (OMNO2)[30].

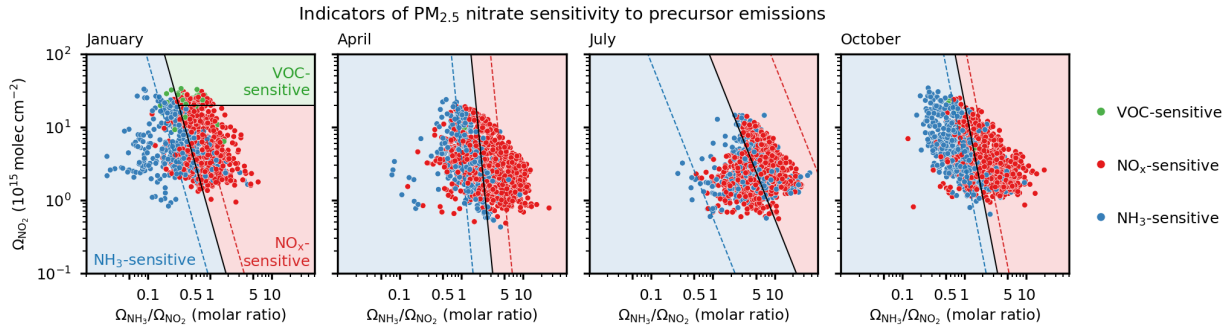

Figure 5: Performance of satellite-based indicator for diagnosing $PM_{2.5}$ nitrate (pNO_3^-) formation sensitivity in the GEOS-Chem model in different seasons. Circles indicate the dominant monthly mean sensitivities of surface pNO_3^- formation (either NH_3-, NO_x-, or VOC-sensitive) in polluted 0.5° × 0.625° model grid cells across East Asia, Europe, and North America (shown in Figure 2). These dominant sensitivities are plotted in an indicator state space as observable from satellite measurements: the $\Omega_{NH3}/\Omega_{NO2}$ column ratio and the Ω_{NO2} column. Ω_{NH3} and Ω_{NO2} columns are sampled to mimic the overpass times of IASI and OMI instruments, respectively. Linear Discriminant Analysis (LDA) establishes thresholds (black solid lines) to separate different regimes, with additional delineations (blue/red dashed

lines) indicating higher confidence levels (>80%) for NH_3- and NO_x-sensitive regimes. Equation (2) with coefficients in Table 1 defines the threshold lines.

Figure 5 shows that application of the satellite-based indicator to diagnose dominant pNO_3^- sensitivities to precursor emissions can be generalized to other regions and seasons. We find similarity of behavior in relating pNO_{3-} sensitivity to the satellite-based indicator for individual regions and therefore all three regions are grouped in Figure 5. Black solid lines, derived using Linear Discriminant Analysis (LDA), delineate transitions between regimes. LDA is a classifier algorithm that finds the linear boundary between classes (https://scikit-learn.org/stable/modules/lda_qda.html). As found under winter conditions in East Asia [39], NH_3-sensitive conditions are associated with $\Omega_{NH3}/\Omega_{NO2}$ ratios below a certain threshold which decreases with increasing Ω_{NO2}. This dependence of the $\Omega_{NH3}/\Omega_{NO2}$ threshold on Ω_{NO2} is due to the reduced efficiency of NO_2 conversion to HNO_3 as NO_x increases, leading to a more likely NH_3 excess at a given $\Omega_{NH3}/\Omega_{NO2}$ ratio. Outside of the NH_3-sensitive regime, whether NO_x or VOCs is the controlling precursor is well delineated by Ω_{NO2} levels. $\Omega_{NO2} > 2 \times 10^{16}$ molec cm^{-2} indicates a strong VOC-limited condition for oxidant formation, making pNO_3^- dominantly sensitive to VOCs emissions (mainly found in winter conditions). For $\Omega_{NO2} < 2 \times 10^{16}$ molec cm^{-2}, the sensitivity is mostly to NO_x emissions.

The ($\Omega_{NH3}/\Omega_{NO2}$, Ω_{NO2}) thresholds shown as black solid lines in Figure 5 diagnose the dominant sensitivity for pNO_3^- formation in GEOS-Chem with an accuracy of 70-80% except in summer. The accuracy rises above 80% for the thresholds defined by dashed lines, indicating high-confidence zones. The lower accuracy in summer is due to: (1) the coexistence of NH_3 and HNO_3 in the gas phase at warmer temperatures, reducing the contrast between sensitivities to NH_3 and NO_2; and (2) increased contributions from the free troposphere to NO_2 column concentrations, making satellite observations less representative of surface conditions [72, 73].

The threshold for separating NH_3- and NO_x-sensitive regimes exhibits seasonal variability, shifting rightward along the $\Omega_{NH3}/\Omega_{NO2}$ axis in warmer seasons. This shift is driven by seasonal variations in the column-to-surface relationship. In warmer seasons, the columns become less representative of surface conditions for both NH_3 and NO_2, due to the increased uplift of surface pollution to the free troposphere and a greater influence of background lightning contributions on the NO_2 columns. The sensitivity regimes, delineated by the solid and dashed lines in Figure 5, are thus diagnosed from $\Omega_{NH3}/\Omega_{NO2}$ and Ω_{NO2} as

$$\text{NH}_3\text{-sensitive:} \quad \log \frac{\Omega_{NH_3}}{\Omega_{NO_2}} < b + k \log \Omega_{NO_2} \quad , \qquad (2a),$$

$$\text{NO}_x\text{-sensitive:} \quad \log \frac{\Omega_{NH_3}}{\Omega_{NO_2}} > b + k \log \Omega_{NO_2} \quad \text{and} \quad \Omega_{NO_2} < y_0 \, , \qquad (2b),$$

$$\text{VOC-sensitive:} \quad \log \frac{\Omega_{NH_3}}{\Omega_{NO_2}} > b + k \log \Omega_{NO_2} \quad \text{and} \quad \Omega_{NO_2} > y_0 \, , \qquad (2c),$$

where the coefficients b, k, and y_0 for different seasons are given in Table 1.

Table 1. Thresholds coefficients for separating pNO_3^- sensitivity regimes in equation 2*.

	Winter (DJF)	Spring (MAM)	Summer (JJA)	Fall (SON)
k	-0.33	-0.13	-0.47	-0.23
$b^{\dagger}$	-0.070	0.40	0.88	0.31
$b_1^{\dagger}$	-0.36	0.08	-0.10	0.12
$b_2^{\dagger}$	0.22	0.71	1.87	0.49
$y_0^{\ddagger}$	20	>20	>20	>20

* With $\Omega_{NH3}/\Omega_{NO2}$ in units of molar ratio and Ω_{NO2} in units of 10^{15} molecules cm^{-2}.

† For thresholding between dominant NH_3- and NO_x-sensitive regimes (b, solid lines in Figure 5), and between high- and low-confidence for a dominant NH_3-sensitive regime (b_1, dashed lines in Figure 5) and a NO_x-sensitive regime (b_2, dashed lines in Figure 5).

‡ No dominant VOC-sensitive conditions were found in the GEOS-Chem simulation for seasons other than winter.

3.2 Application to satellite observations

We now diagnose local pNO_3^- sensitivity regimes across East Asia, Europe, and North America for different seasons in 2017 by applying the model thresholds from Equation 2 to the OMI and IASI satellite observations of ($\Omega_{NH3}/\Omega_{NO2}$, Ω_{NO2}) as shown in Figures 2 and 4. Figure 6 shows the spatial distribution of the dominant sensitivities to emissions inferred from the satellite indicator. Winter data in Europe are sparse due to low number of successful NH_3 retrievals [74].

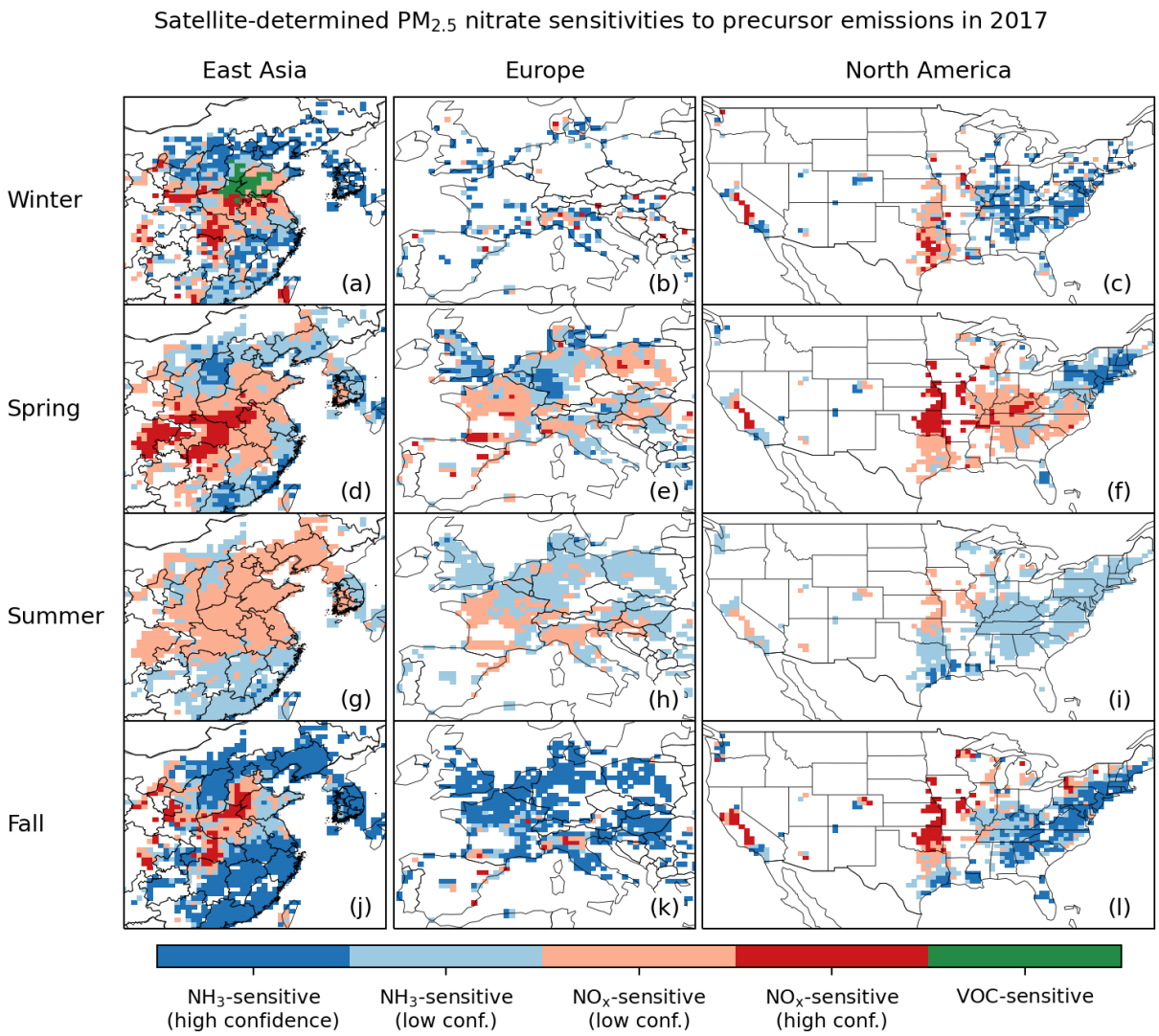

Figure 6: Dominant sensitivities of $PM_{2.5}$ nitrate (pNO_3^-) to precursor emissions in East Asia, Europe, and North America in 2017 as diagnosed from seasonal mean IASI and OMI satellite observations of tropospheric NH_3 and NO_2 columns. The regimes are diagnosed using the threshold lines from Figure 5 (Equation (2) with coefficients from Table 1). White areas indicate either lack of data or remote areas (winter $\Omega_{NO2} < 2.5 \times 10^{15}$ molec cm^{-2}).

The satellite measurements indicate varying pNO_3^- sensitivity regimes across regions. Focusing on winter when pNO_3^- pollution is most severe (first row of Figure 6), NH_3-sensitive regimes are identified in areas with relatively low $\Omega_{NH3}/\Omega_{NO2}$ ratios. These include the northern North China Plain (NCP, including Beijing), the Yangtze River Delta (YRD, including Shanghai), the Seoul Metropolitan Area (SMA), most of Europe, Los Angeles, and the eastern US. In these regions, reducing NH_3 emissions is the most effective method to reduce winter pNO_3^- concentrations. NO_x-sensitive regimes are identified in areas

with higher $\Omega_{NH3}/\Omega_{NO2}$ ratios and relatively low Ω_{NO2} including central China (Fen-Wei Plain, Sichuan Basin, and Hubei and Hunan provinces), the Po Valley in Italy, the central US, and the Central Valley in California. These are agricultural areas with high NH_3 emissions even in winter, so that reducing NO_x emissions is most effective for controlling winter pNO_3^- levels. Dominant VOC-sensitive conditions are found in the southern NCP, characterized by both NH_3 saturation ($\Omega_{NH3}/\Omega_{NO2}$ ratio > 0.4, Fig. 4) and very high Ω_{NO2} (> 2×10^{16} molec cm^{-2}, Fig. 2). In this region, the most effective approach to decrease winter pNO_3^- is to control VOC emissions.

Both $\Omega_{NH3}/\Omega_{NO2}$ and Ω_{NO2} exhibit significant seasonal variations, as discussed in Section 2.2. The $\Omega_{NH3}/\Omega_{NO2}$ ratio is lowest in winter and highest in summer, while Ω_{NO2} shows the opposite pattern. Despite these variations, the spatial pattern of dominant sensitivities, specifically NO_x- and NH_3-sensitive regions, remains largely consistent throughout the year. This is because of the shift in the demarcation between regimes in Figure 5. Ω_{NO2} may be low in summer but the HNO_3 production rate is larger than in winter. The VOC-sensitive regime is limited to winter, as would be expected because VOC limitation of oxidant chemistry is weaker in other seasons.

3.3 Comparisons to local studies

Tables 2 compares the pNO_3^- sensitivities identified from the satellite indicator with results from local studies in East Asia, Europe, and the US. We collect three kinds of local studies from the literature: 1) field studies that measure gas and aerosol concentrations and use observational indicators or thermodynamic models to identify the dominant sensitivities; 2) COVID studies that examine the response of pNO_3^- levels to real-world NO_x reductions during the COVID-19 pandemic; 3) regional CTM studies that quantify the response of pNO_3^- levels to perturbed precursor emissions of NO_x, NH_3, or VOCs. Most of the studies focused on only one season. The field studies diagnose NH_3 and HNO_3 sensitivities, and some relate HNO_3 sensitivities to NO_x and VOC emissions using an oxidant chemistry model. HNO_3 sensitivity generally implies sensitivity to NO_x emissions except under urban winter conditions where it implies sensitivity to VOC emissions [24]. The COVID studies diagnose whether or not pNO_3^- is sensitive to NO_x emission reductions [66, 75, 76].

Our results align in general very well with these local studies, which find pNO_3^- formation to be NH_3-sensitive in Guangzhou (fall) [77], Germany (spring) [76], the Northeast US (winter), the Southeast US (summer), and Los Angeles (summer) [14]; and to be HNO_3-sensitive in Jinan, NCP (summer) [78], central China (all seasons) [75, 79], the Po Valley (all seasons) [80], Paris (spring) [81], and the Central Valley in

California (winter) [82-84]. Our satellite-based indicator can successfully distinguish spatial contrasts between NH_3-sensitive and NO_x-sensitive regions, and the consistency in regimes across seasons also agrees well with previous local studies. Using the WRF-Chem model, Li, et al. [28] found an increased sensitivity to NO_x during summer in the NCP and YRD, due to a shift to transitional/NO_x-sensitive regime for oxidant formation. We also find a larger area of NO_x-sensitive conditions in eastern China in summer. Summertime pNO_3^- is important in China where it can contribute to pollution episodes [85, 86].

Table 2a. Comparison to previous studies of $PM_{2.5}$ nitrate sensitivity in East Asia.

Previous study	Season	Study type	Finding	This work
North China Plain				
Regional [10, 12, 28]	Winter	CTM	NH_3- and VOC-sensitive	NH_3- and VOC-sensitive
Regional [28]	Summer	CTM	NO_x- and NH_3-sensitive	NO_x-sensitive
Beijing [14, 75]	Winter	Field COVID	HNO_3-sensitive but NO_x-insensitive	NH_3-sensitive
Jinan [78]	Summer	Field	HNO_3-sensitive	NO_x-sensitive
Yangtze River Delta				
Regional [28, 87]	Winter	CTM	NH_3-sensitive	NH_3-sensitive
Regional [28]	Summer	CTM	NH_3-sensitive	NH_3- and NO_x-sensitive
Nanjing [75, 88]	Winter	Field COVID	HNO_3-sensitive but NO_x-insensitive	NH_3-sensitive
Shanghai [66]	Winter	Field COVID	HNO_3-sensitive but NO_x-insensitive	NH_3-sensitive
Central China				
Changsha [75]	Winter	COVID	NO_x-sensitive	NO_x-sensitive
Wuhan [79]	All seasons	Field	HNO_3-sensitive	NO_x-sensitive
South China				
Guangzhou [77]	Fall	Field	NH_3-sensitive	NH_3-sensitive

Table 2b. Same as Table 2a but for Europe.

Previous study	Season	Study type	Finding	This work
Cabauw, Netherlands [14]	All seasons	Field	HNO_3-sensitive	NH_3-sensitive
Po Valley, Italy [80]	All seasons	Field	HNO_3-sensitive	NO_x-sensitive
Paris, France [81]	Spring	COVID	NO_x-sensitive	NO_x-sensitive
Germany [76]	Spring	COVID	NO_x-insensitive	NH_3-sensitive

Table 2c. Same as Table 2a but for the United States (US).

Previous study	Season	Study type	Finding	This work
Northeast US				
Regional [14]	Winter	Field	NH_3-sensitive	NH_3-sensitive
Western US				
Salt Lake City [4, 24]	Winter	Field	HNO_3-sensitive, VOC-sensitive	NH_3-sensitive
Central Valley [82-84]	Winter	Field	HNO_3-sensitive	NO_x-sensitive
Los Angeles [14]	Summer	Field	NH_3-sensitive	NH_3-sensitive
Southeast US				
Regional [14]	Summer	Field	NH_3-sensitive	NH_3-sensitive

Some urban field studies in winter including in Beijing, Nanjing, Shanghai, and Salt Lake City concluded that pNO_3^- formation is more sensitive to HNO_3 than NH_3 due to an observed excess of NH_3 [4, 14, 66, 88]. However, we find these environments to be dominantly NH_3-sensitive. This may be explained by differences in the lifetimes of HNO_3 and pNO_3^- against deposition that drive greater sensitivity to NH_3 even when NH_3 concentrations are in excess [10, 21, 39]. CTM studies for urban winter conditions, which would include the deposition effect, report results consistent with ours, including dominant sensitivities to NH_3 and VOC emissions in the NCP [10, 12, 28] and to NH_3 in the YRD [28]. One discrepancy that we cannot explain is for Cabauw (Netherlands), where a field study indicates a HNO_3-sensitive regime in all seasons [14], while our satellite indicator finds a NH_3-sensitive regime.

In summary, we have shown that a new satellite-based indicator using measurements of NO_2 and NH_3 columns can effectively diagnose the sensitivity of $PM_{2.5}$ nitrate formation to NO_x, NH_3, and VOC emissions in polluted regions of East Asia, Europe, and North America across all seasons. We demonstrated the effectiveness of the indicator in the GEOS-Chem model and derived thresholds to demarcate the dominant sensitivity regimes in different seasons. By applying this method to OMI NO_2 and IASI NH_3 observations, we found that some regions are dominantly NO_x-sensitive while others are dominantly NH_3-sensitive, consistently across seasons. VOC-sensitive conditions are limited to urban areas in winter with high NH_3 and very high NO_2. We compared our satellite-determined regimes with previous local studies and found good consistency. Our results emphasize the need for tailored emission control strategies to mitigate $PM_{2.5}$ nitrate pollution. The accuracy of our satellite-based indicator should improve with NO_2 and NH_3 measurements from the same platform as is planned for the geostationary satellites Sentinel-4 [34] over Europe and GeoXO over North America [89], as well as the proposed Nitrosat mission [90].

AUTHOR INFORMATION

Corresponding Author

Ruijun Dang - *John A. Paulson School of Engineering and Applied Sciences, Harvard University, Cambridge, MA 02138, USA*. Email: rjdang@g.harvard.edu

Author Contributions

RD and DJJ designed the study. RD conducted model simulations and data analysis, with contributions from DJJ, SZ, LHY, and DCP. PC, LC, and MVD provided guidance on the analysis of the NH_3 satellite product. DCP, JC, JP, ZL, HL, and PX contributed to the measurement/collection of $PM_{2.5}$ composition data. RD led the writing with contributions from all authors.

Funding Sources

This work was supported by the Harvard–NUIST Joint Laboratory for Air Quality and Climate. The research in Belgium was supported by the Belgian Science Policy Office (BELSPO, Prodex HIRS and FED-tWIN ARENBERG projects) and the Air Liquide Foundation (TAPIR project). L. Clarisse is Research Associate supported by the Belgian F.R.S.-FNRS).

Notes

The authors declare that they have no conflict of interest.

REFERENCES

(1) Tian, M.; Liu, Y.; Yang, F.; Zhang, L.; Peng, C.; Chen, Y.; Shi, G.; Wang, H.; Luo, B.; Jiang, C.; et al. Increasing importance of nitrate formation for heavy aerosol pollution in two megacities in Sichuan Basin, southwest China. *Environ. Pollut.* **2019**, *250*, 898-905. DOI: https://doi.org/10.1016/j.envpol.2019.04.098.

(2) Li, H.; Zhang, Q.; Zheng, B.; Chen, C.; Wu, N.; Guo, H.; Zhang, Y.; Zheng, Y.; Li, X.; He, K. Nitrate-driven urban haze pollution during summertime over the North China Plain. *Atmos. Chem. Phys.* **2018**, *18* (8), 5293-5306. DOI: 10.5194/acp-18-5293-2018.

(3) Foret, G.; Michoud, V.; Kotthaus, S.; Petit, J. E.; Baudic, A.; Siour, G.; Kim, Y.; Doussin, J. F.; Dupont, J. C.; Formenti, P.; et al. The December 2016 extreme weather and particulate matter pollution episode in the Paris region (France). *Atmos. Environ.* **2022**, *291*, 119386. DOI: https://doi.org/10.1016/j.atmosenv.2022.119386.

(4) Franchin, A.; Fibiger, D. L.; Goldberger, L.; McDuffie, E. E.; Moravek, A.; Womack, C. C.; Crosman, E. T.; Docherty, K. S.; Dube, W. P.; Hoch, S. W.; et al. Airborne and ground-based observations of ammonium-nitrate-dominated aerosols in a shallow boundary layer during intense winter pollution episodes in northern Utah. *Atmos. Chem. Phys.* **2018**, *18* (23), 17259-17276. DOI: 10.5194/acp-18-17259-2018.

(5) Zhang, Y.; Tian, J.; Wang, Q.; Qi, L.; Manousakas, M. I.; Han, Y.; Ran, W.; Sun, Y.; Liu, H.; Zhang, R.; et al. High-time-resolution chemical composition and source apportionment of PM2.5 in northern Chinese cities: implications for policy. *Atmos. Chem. Phys.* **2023**, *23* (16), 9455-9471. DOI: 10.5194/acp-23-9455-2023.

(6) Attwood, A. R.; Washenfelder, R. A.; Brock, C. A.; Hu, W.; Baumann, K.; Campuzano-Jost, P.; Day, D. A.; Edgerton, E. S.; Murphy, D. M.; Palm, B. B.; et al. Trends in sulfate and organic aerosol mass in the Southeast U.S.: Impact on aerosol optical depth and radiative forcing. *Geophys. Res. Lett.* **2014**, *41* (21), 7701-7709, https://doi.org/10.1002/2014GL061669. DOI: https://doi.org/10.1002/2014GL061669 (acccessed 2023/05/19).

(7) Zhai, S.; Jacob, D. J.; Wang, X.; Shen, L.; Li, K.; Zhang, Y.; Gui, K.; Zhao, T.; Liao, H. Fine particulate matter (PM2.5) trends in China, 2013–2018: separating contributions from anthropogenic emissions and meteorology. *Atmos. Chem. Phys.* **2019**, *19* (16), 11031-11041. DOI: 10.5194/acp-19-11031-2019.

(8) Li, H.; Cheng, J.; Zhang, Q.; Zheng, B.; Zhang, Y.; Zheng, G.; He, K. Rapid transition in winter aerosol composition in Beijing from 2014 to 2017: response to clean air actions. *Atmos. Chem. Phys.* **2019**, *19* (17), 11485-11499. DOI: 10.5194/acp-19-11485-2019.

(9) Shah, V.; Jaegle, L.; Thornton, J. A.; Lopez-Hilfiker, F. D.; Lee, B. H.; Schroder, J. C.; Campuzano-Jost, P.; Jimenez, J. L.; Guo, H. Y.; Sullivan, A. P.; et al. Chemical feedbacks weaken the wintertime response of particulate sulfate and nitrate to emissions reductions over the eastern United States. *Proc. Natl. Acad. Sci. U. S. A.* **2018**, *115* (32), 8110-8115, Article. DOI: 10.1073/pnas.1803295115.

(10) Zhai, S.; Jacob, D. J.; Wang, X.; Liu, Z.; Wen, T.; Shah, V.; Li, K.; Moch, J. M.; Bates, K. H.; Song, S.; et al. Control of particulate nitrate air pollution in China. *Nat. Geosci.* **2021**, *14* (6), 389-395. DOI: 10.1038/s41561-021-00726-z.

(11) Chuang, M.-T.; Chou, C. C. K.; Hsiao, T.-C.; Lin, K.-y.; Lin, N.-H.; Lin, W.-Y.; Wang, S.-H.; Pani, S. K.; Lee, C.-T. Analyzing the increasing importance of nitrate in Taiwan from long-term trend of measurements. *Atmos. Environ.* **2021**, *267*, 118749. DOI: https://doi.org/10.1016/j.atmosenv.2021.118749.

(12) Fu, X.; Wang, T.; Gao, J.; Wang, P.; Liu, Y.; Wang, S.; Zhao, B.; Xue, L. Persistent Heavy Winter Nitrate Pollution Driven by Increased Photochemical Oxidants in Northern China. *Environ. Sci. Technol.* **2020**, *54* (7), 3881-3889. DOI: 10.1021/acs.est.9b07248.

(13) Song, S. J.; Nenes, A.; Gao, M.; Zhang, Y. Z.; Liu, P. F.; Shao, J. Y.; Ye, D. C.; Xu, W. Q.; Lei, L.; Sun, Y. L.; et al. Thermodynamic Modeling Suggests Declines in Water Uptake and Acidity of Inorganic Aerosols in Beijing Winter Haze Events during 2014/2015-2018/2019. *Environ. Sci. Technol. Lett.* **2019**, *6* (12), 752-760, Article. DOI: 10.1021/acs.estlett.9b00621.

(14) Guo, H.; Otjes, R.; Schlag, P.; Kiendler-Scharr, A.; Nenes, A.; Weber, R. J. Effectiveness of ammonia reduction on control of fine particle nitrate. *Atmos. Chem. Phys.* **2018**, *18* (16), 12241-12256. DOI: 10.5194/acp-18-12241-2018.

(15) Zhang, L.; Jacob, D. J.; Knipping, E. M.; Kumar, N.; Munger, J. W.; Carouge, C. C.; van Donkelaar, A.; Wang, Y. X.; Chen, D. Nitrogen deposition to the United States: distribution, sources, and processes. *Atmos. Chem. Phys.* **2012**, *12* (10), 4539-4554. DOI: 10.5194/acp-12-4539-2012.

(16) Liu, L.; Xu, W.; Lu, X.; Zhong, B.; Guo, Y.; Lu, X.; Zhao, Y.; He, W.; Wang, S.; Zhang, X.; et al. Exploring global changes in agricultural ammonia emissions and their contribution to nitrogen deposition since 1980. *Proceedings of the National Academy of Sciences* **2022**, *119* (14), e2121998119. DOI: doi:10.1073/pnas.2121998119.

(17) Van Damme, M.; Clarisse, L.; Whitburn, S.; Hadji-Lazaro, J.; Hurtmans, D.; Clerbaux, C.; Coheur, P.-F. Industrial and agricultural ammonia point sources exposed. *Nature* **2018**, *564* (7734), 99-103. DOI: 10.1038/s41586-018-0747-1.
(18) Chen, Y.; Zhang, Q.; Cai, X.; Zhang, H.; Lin, H.; Zheng, C.; Guo, Z.; Hu, S.; Chen, L.; Tao, S.; et al. Rapid Increase in China's Industrial Ammonia Emissions: Evidence from Unit-Based Mapping. *Environ. Sci. Technol.* **2022**, *56* (6), 3375-3385. DOI: 10.1021/acs.est.1c08369.
(19) Farren, N. J.; Davison, J.; Rose, R. A.; Wagner, R. L.; Carslaw, D. C. Underestimated Ammonia Emissions from Road Vehicles. *Environ. Sci. Technol.* **2020**, *54* (24), 15689-15697. DOI: 10.1021/acs.est.0c05839.
(20) Shen, L.; Jacob, D. J.; Zhu, L.; Zhang, Q.; Zheng, B.; Sulprizio, M. P.; Li, K.; De Smedt, I.; González Abad, G.; Cao, H.; et al. The 2005–2016 Trends of Formaldehyde Columns Over China Observed by Satellites: Increasing Anthropogenic Emissions of Volatile Organic Compounds and Decreasing Agricultural Fire Emissions. *Geophys. Res. Lett.* **2019**, *46* (8), 4468-4475. DOI: https://doi.org/10.1029/2019GL082172.
(21) Nenes, A.; Pandis, S. N.; Weber, R. J.; Russell, A. Aerosol pH and liquid water content determine when particulate matter is sensitive to ammonia and nitrate availability. *Atmos. Chem. Phys.* **2020**, *20* (5), 3249-3258. DOI: 10.5194/acp-20-3249-2020.
(22) Petetin, H.; Sciare, J.; Bressi, M.; Gros, V.; Rosso, A.; Sanchez, O.; Sarda-Estève, R.; Petit, J. E.; Beekmann, M. Assessing the ammonium nitrate formation regime in the Paris megacity and its representation in the CHIMERE model. *Atmos. Chem. Phys.* **2016**, *16* (16), 10419-10440. DOI: 10.5194/acp-16-10419-2016.
(23) Xu, Z.; Liu, M.; Zhang, M.; Song, Y.; Wang, S.; Zhang, L.; Xu, T.; Wang, T.; Yan, C.; Zhou, T.; et al. High efficiency of livestock ammonia emission controls in alleviating particulate nitrate during a severe winter haze episode in northern China. *Atmos. Chem. Phys.* **2019**, *19* (8), 5605-5613. DOI: 10.5194/acp-19-5605-2019.
(24) Womack, C. C.; McDuffie, E. E.; Edwards, P. M.; Bares, R.; de Gouw, J. A.; Docherty, K. S.; Dubé, W. P.; Fibiger, D. L.; Franchin, A.; Gilman, J. B.; et al. An Odd Oxygen Framework for Wintertime Ammonium Nitrate Aerosol Pollution in Urban Areas: NOx and VOC Control as Mitigation Strategies. *Geophys. Res. Lett.* **2019**, *46* (9), 4971-4979. DOI: https://doi.org/10.1029/2019GL082028.
(25) Romer Present, P. S.; Zare, A.; Cohen, R. C. The changing role of organic nitrates in the removal and transport of NOx. *Atmos. Chem. Phys.* **2020**, *20* (1), 267-279. DOI: 10.5194/acp-20-267-2020.
(26) Zhai, S.; Jacob, D. J.; Pendergrass, D. C.; Colombi, N. K.; Shah, V.; Yang, L. H.; Zhang, Q.; Wang, S.; Kim, H.; Sun, Y.; et al. Coarse particulate matter air quality in East Asia: implications for fine particulate nitrate. *Atmos. Chem. Phys.* **2023**, *23* (7), 4271-4281. DOI: 10.5194/acp-23-4271-2023.
(27) Ansari, A. S.; Pandis, S. N. Response of Inorganic PM to Precursor Concentrations. *Environ. Sci. Technol.* **1998**, *32* (18), 2706-2714. DOI: 10.1021/es971130j.
(28) Li, M.; Zhang, Z.; Yao, Q.; Wang, T.; Xie, M.; Li, S.; Zhuang, B.; Han, Y. Nonlinear responses of particulate nitrate to NOx emission controls in the megalopolises of China. *Atmos. Chem. Phys.* **2021**, *21* (19), 15135-15152. DOI: 10.5194/acp-21-15135-2021.
(29) Martin, R. V.; Chance, K.; Jacob, D. J.; Kurosu, T. P.; Spurr, R. J. D.; Bucsela, E.; Gleason, J. F.; Palmer, P. I.; Bey, I.; Fiore, A. M.; et al. An improved retrieval of tropospheric nitrogen dioxide from GOME. *Journal of Geophysical Research: Atmospheres* **2002**, *107* (D20), ACH 9-1-ACH 9-21, https://doi.org/10.1029/2001JD001027. DOI: https://doi.org/10.1029/2001JD001027 (acccessed 2022/04/21).
(30) Lamsal, L. N.; Krotkov, N. A.; Vasilkov, A.; Marchenko, S.; Qin, W.; Yang, E. S.; Fasnacht, Z.; Joiner, J.; Choi, S.; Haffner, D.; et al. Ozone Monitoring Instrument (OMI) Aura nitrogen dioxide standard product version 4.0 with improved surface and cloud treatments. *Atmos. Meas. Tech.* **2021**, *14* (1), 455-479. DOI: 10.5194/amt-14-455-2021.
(31) van Geffen, J.; Boersma, K. F.; Eskesl, H.; Sneep, M.; ter Linden, M.; Zara, M.; Veefkind, J. P. S5P TROPOMI NO2 slant column retrieval: method, stability, uncertainties and comparisons with OMI. *Atmos. Meas. Tech.* **2020**, *13* (3), 1315-1335. DOI: 10.5194/amt-13-1315-2020.

(32) Kim, J.; Jeong, U.; Ahn, M.-H.; Kim, J. H.; Park, R. J.; Lee, H.; Song, C. H.; Choi, Y.-S.; Lee, K.-H.; Yoo, J.-M.; et al. New Era of Air Quality Monitoring from Space: Geostationary Environment Monitoring Spectrometer (GEMS). *Bull. Amer. Meteorol. Soc.* **2020**, *101* (1), E1-E22. DOI: https://doi.org/10.1175/BAMS-D-18-0013.1.
(33) Zoogman, P.; Liu, X.; Suleiman, R. M.; Pennington, W. F.; Flittner, D. E.; Al-Saadi, J. A.; Hilton, B. B.; Nicks, D. K.; Newchurch, M. J.; Carr, J. L.; et al. Tropospheric emissions: Monitoring of pollution (TEMPO). *Journal of Quantitative Spectroscopy and Radiative Transfer* **2017**, *186*, 17-39. DOI: https://doi.org/10.1016/j.jqsrt.2016.05.008.
(34) Gulde, S.; Kolm, M.; Smith, D.; Maurer, R.; Bazalgette Courrèges-Lacoste, G.; Sallusti, M.; Bagnasco, G. *Sentinel 4: a geostationary imaging UVN spectrometer for air quality monitoring: status of design, performance and development*; SPIE, 2017.
(35) Beer, R.; Shephard, M. W.; Kulawik, S. S.; Clough, S. A.; Eldering, A.; Bowman, K. W.; Sander, S. P.; Fisher, B. M.; Payne, V. H.; Luo, M.; et al. First satellite observations of lower tropospheric ammonia and methanol. *Geophys. Res. Lett.* **2008**, *35* (9). DOI: https://doi.org/10.1029/2008GL033642.
(36) Clarisse, L.; Clerbaux, C.; Dentener, F.; Hurtmans, D.; Coheur, P.-F. Global ammonia distribution derived from infrared satellite observations. *Nat. Geosci.* **2009**, *2* (7), 479-483. DOI: 10.1038/ngeo551.
(37) Shephard, M. W.; Cady-Pereira, K. E. Cross-track Infrared Sounder (CrIS) satellite observations of tropospheric ammonia. *Atmos. Meas. Tech.* **2015**, *8* (3), 1323-1336. DOI: 10.5194/amt-8-1323-2015.
(38) Lamarre, D.; Aminou, D.; van den Braembussche, P.; Hallibert, P.; Ahlers, B.; Wilson, M.; Luhmann, H. J. Meteosat Third Generation: The Infrared Sounder Instrument. In *Imaging and Applied Optics*, Toronto, 2011/07/10, 2011; Optica Publishing Group: p JMA2.
(39) Dang, R.; Jacob, D. J.; Zhai, S.; Coheur, P.; Clarisse, L.; Van Damme, M.; Pendergrass, D. C.; Choi, J.-s.; Park, J.-s.; Liu, Z.; et al. Diagnosing the Sensitivity of Particulate Nitrate to Precursor Emissions Using Satellite Observations of Ammonia and Nitrogen Dioxide. *Geophys. Res. Lett.* **2023**, *50* (24), e2023GL105761. DOI: https://doi.org/10.1029/2023GL105761.
(40) Jin, X.; Fiore, A. M.; Murray, L. T.; Valin, L. C.; Lamsal, L. N.; Duncan, B.; Folkert Boersma, K.; De Smedt, I.; Abad, G. G.; Chance, K.; et al. Evaluating a Space-Based Indicator of Surface Ozone-NOx-VOC Sensitivity Over Midlatitude Source Regions and Application to Decadal Trends. *Journal of Geophysical Research: Atmospheres* **2017**, *122* (19), 10,439-410,461. DOI: https://doi.org/10.1002/2017JD026720 (acccessed 2023/08/17).
(41) Martin, R. V.; Fiore, A. M.; Van Donkelaar, A. Space-based diagnosis of surface ozone sensitivity to anthropogenic emissions. *Geophys. Res. Lett.* **2004**, *31* (6), https://doi.org/10.1029/2004GL019416. DOI: https://doi.org/10.1029/2004GL019416 (acccessed 2022/05/15).
(42) Duncan, B. N.; Yoshida, Y.; Olson, J. R.; Sillman, S.; Martin, R. V.; Lamsal, L.; Hu, Y.; Pickering, K. E.; Retscher, C.; Allen, D. J.; et al. Application of OMI observations to a space-based indicator of NOx and VOC controls on surface ozone formation. *Atmos. Environ.* **2010**, *44* (18), 2213-2223. DOI: https://doi.org/10.1016/j.atmosenv.2010.03.010.
(43) Zhu, L.; Jacob, D. J.; Mickley, L. J.; Marais, E. A.; Cohan, D. S.; Yoshida, Y.; Duncan, B. N.; González Abad, G.; Chance, K. V. Anthropogenic emissions of highly reactive volatile organic compounds in eastern Texas inferred from oversampling of satellite (OMI) measurements of HCHO columns. *Environ. Res. Lett.* **2014**, *9* (11), 114004. DOI: 10.1088/1748-9326/9/11/114004.
(44) Wang, X.; Jacob, D. J.; Downs, W.; Zhai, S.; Zhu, L.; Shah, V.; Holmes, C. D.; Sherwen, T.; Alexander, B.; Evans, M. J.; et al. Global tropospheric halogen (Cl, Br, I) chemistry and its impact on oxidants. *Atmos. Chem. Phys.* **2021**, *21* (18), 13973-13996. DOI: 10.5194/acp-21-13973-2021.
(45) Fountoukis, C.; Nenes, A. ISORROPIA II: a computationally efficient thermodynamic equilibrium model for K+-Ca2+-Mg2+-Nh(4)(+)-Na+-SO42--NO3--Cl--H2O aerosols. *Atmospheric Chemistry and Physics* **2007**, *7* (17), 4639-4659, Article. DOI: 10.5194/acp-7-4639-2007.
(46) Fisher, J. A.; Jacob, D. J.; Travis, K. R.; Kim, P. S.; Marais, E. A.; Chan Miller, C.; Yu, K.; Zhu, L.; Yantosca, R. M.; Sulprizio, M. P.; et al. Organic nitrate chemistry and its implications for nitrogen budgets in an isoprene- and monoterpene-rich atmosphere: constraints from aircraft (SEAC4RS) and

ground-based (SOAS) observations in the Southeast US. *Atmos. Chem. Phys.* **2016**, *16* (9), 5969-5991. DOI: 10.5194/acp-16-5969-2016.
(47) Alexander, B.; Park, R. J.; Jacob, D. J.; Li, Q. B.; Yantosca, R. M.; Savarino, J.; Lee, C. C. W.; Thiemens, M. H. Sulfate formation in sea-salt aerosols: Constraints from oxygen isotopes. *Journal of Geophysical Research: Atmospheres* **2005**, *110* (D10). DOI: https://doi.org/10.1029/2004JD005659.
(48) Fairlie, T. D.; Jacob, D. J.; Dibb, J. E.; Alexander, B.; Avery, M. A.; van Donkelaar, A.; Zhang, L. Impact of mineral dust on nitrate, sulfate, and ozone in transpacific Asian pollution plumes. *Atmos. Chem. Phys.* **2010**, *10* (8), 3999-4012. DOI: 10.5194/acp-10-3999-2010.
(49) Heald, C. L.; Collett Jr, J. L.; Lee, T.; Benedict, K. B.; Schwandner, F. M.; Li, Y.; Clarisse, L.; Hurtmans, D. R.; Van Damme, M.; Clerbaux, C.; et al. Atmospheric ammonia and particulate inorganic nitrogen over the United States. *Atmos. Chem. Phys.* **2012**, *12* (21), 10295-10312. DOI: 10.5194/acp-12-10295-2012.
(50) Bian, H.; Chin, M.; Hauglustaine, D. A.; Schulz, M.; Myhre, G.; Bauer, S. E.; Lund, M. T.; Karydis, V. A.; Kucsera, T. L.; Pan, X.; et al. Investigation of global particulate nitrate from the AeroCom phase III experiment. *Atmos. Chem. Phys.* **2017**, *17* (21), 12911-12940. DOI: 10.5194/acp-17-12911-2017.
(51) Luo, G.; Yu, F.; Schwab, J. Revised treatment of wet scavenging processes dramatically improves GEOS-Chem 12.0.0 simulations of surface nitric acid, nitrate, and ammonium over the United States. *Geosci. Model Dev.* **2019**, *12* (8), 3439-3447. DOI: 10.5194/gmd-12-3439-2019.
(52) Luo, G.; Yu, F.; Moch, J. M. Further improvement of wet process treatments in GEOS-Chem v12.6.0: impact on global distributions of aerosols and aerosol precursors. *Geosci. Model Dev.* **2020**, *13* (6), 2879-2903. DOI: 10.5194/gmd-13-2879-2020.
(53) Dang, R.; Jacob, D. J.; Shah, V.; Eastham, S. D.; Fritz, T. M.; Mickley, L. J.; Liu, T.; Wang, Y.; Wang, J. Background nitrogen dioxide (NO2) over the United States and its implications for satellite observations and trends: effects of nitrate photolysis, aircraft, and open fires. *Atmos. Chem. Phys.* **2023**, *23* (11), 6271-6284. DOI: 10.5194/acp-23-6271-2023.
(54) McDuffie, E. E.; Smith, S. J.; O'Rourke, P.; Tibrewal, K.; Venkataraman, C.; Marais, E. A.; Zheng, B.; Crippa, M.; Brauer, M.; Martin, R. V. A global anthropogenic emission inventory of atmospheric pollutants from sector- and fuel-specific sources (1970–2017): an application of the Community Emissions Data System (CEDS). *Earth Syst. Sci. Data* **2020**, *12* (4), 3413-3442. DOI: 10.5194/essd-12-3413-2020.
(55) Zheng, B.; Tong, D.; Li, M.; Liu, F.; Hong, C.; Geng, G.; Li, H.; Li, X.; Peng, L.; Qi, J.; et al. Trends in China's anthropogenic emissions since 2010 as the consequence of clean air actions. *Atmos. Chem. Phys. Discuss.* **2018**, *2018*, 1-27. DOI: 10.5194/acp-2018-374.
(56) Woo, J.-H.; Kim, Y.; Kim, H.-K.; Choi, K.-C.; Eum, J.-H.; Lee, J.-B.; Lim, J.-H.; Kim, J.; Seong, M. Development of the CREATE Inventory in Support of Integrated Climate and Air Quality Modeling for Asia. *Sustainability* **2020**, *12* (19), 7930.
(57) Huang, X.; Liu, Z.; Liu, J.; Hu, B.; Wen, T.; Tang, G.; Zhang, J.; Wu, F.; Ji, D.; Wang, L.; et al. Chemical characterization and source identification of PM2.5 at multiple sites in the Beijing–Tianjin–Hebei region, China. *Atmos. Chem. Phys.* **2017**, *17* (21), 12941-12962. DOI: 10.5194/acp-17-12941-2017.
(58) Liu, Z.; Gao, W.; Yu, Y.; Hu, B.; Xin, J.; Sun, Y.; Wang, L.; Wang, G.; Bi, X.; Zhang, G.; et al. Characteristics of PM2.5 mass concentrations and chemical species in urban and background areas of China: emerging results from the CARE-China network. *Atmos. Chem. Phys.* **2018**, *18* (12), 8849-8871. DOI: 10.5194/acp-18-8849-2018.
(59) Tan, T.; Hu, M.; Li, M.; Guo, Q.; Wu, Y.; Fang, X.; Gu, F.; Wang, Y.; Wu, Z. New insight into PM2.5 pollution patterns in Beijing based on one-year measurement of chemical compositions. *Sci. Total Environ.* **2018**, *621*, 734-743. DOI: https://doi.org/10.1016/j.scitotenv.2017.11.208.
(60) Zhang, Q.; Zheng, Y.; Tong, D.; Shao, M.; Wang, S.; Zhang, Y.; Xu, X.; Wang, J.; He, H.; Liu, W.; et al. Drivers of improved PM_{2.5} air quality in China from 2013 to 2017. *Proceedings of the National Academy of Sciences* **2019**, *116* (49), 24463-24469. DOI: doi:10.1073/pnas.1907956116.

(61) Zhao, L.; Wang, L.; Tan, J.; Duan, J.; Ma, X.; Zhang, C.; Ji, S.; Qi, M.; Lu, X.; Wang, Y.; et al. Changes of chemical composition and source apportionment of PM2.5 during 2013–2017 in urban Handan, China. *Atmos. Environ.* **2019**, *206*, 119-131. DOI: https://doi.org/10.1016/j.atmosenv.2019.02.034.
(62) Kong, L.; Feng, M.; Liu, Y.; Zhang, Y.; Zhang, C.; Li, C.; Qu, Y.; An, J.; Liu, X.; Tan, Q.; et al. Elucidating the pollution characteristics of nitrate, sulfate and ammonium in PM2.5 in Chengdu, southwest China, based on 3-year measurements. *Atmos. Chem. Phys.* **2020**, *20* (19), 11181-11199. DOI: 10.5194/acp-20-11181-2020.
(63) Chow, W. S.; Liao, K.; Huang, X. H. H.; Leung, K. F.; Lau, A. K. H.; Yu, J. Z. Measurement report: The 10-year trend of PM2.5 major components and source tracers from 2008 to 2017 in an urban site of Hong Kong, China. *Atmos. Chem. Phys.* **2022**, *22* (17), 11557-11577. DOI: 10.5194/acp-22-11557-2022.
(64) Sun, J.; Qin, M.; Xie, X.; Fu, W.; Qin, Y.; Sheng, L.; Li, L.; Li, J.; Sulaymon, I. D.; Jiang, L.; et al. Seasonal modeling analysis of nitrate formation pathways in Yangtze River Delta region, China. *Atmos. Chem. Phys.* **2022**, *22* (18), 12629-12646. DOI: 10.5194/acp-22-12629-2022.
(65) Xie, M.; Lu, X.; Ding, F.; Cui, W.; Zhang, Y.; Feng, W. Evaluating the influence of constant source profile presumption on PMF analysis of PM2.5 by comparing long- and short-term hourly observation-based modeling. *Environ. Pollut.* **2022**, *314*, 120273. DOI: https://doi.org/10.1016/j.envpol.2022.120273.
(66) Zang, H.; Zhao, Y.; Huo, J.; Zhao, Q.; Fu, Q.; Duan, Y.; Shao, J.; Huang, C.; An, J.; Xue, L.; et al. High atmospheric oxidation capacity drives wintertime nitrate pollution in the eastern Yangtze River Delta of China. *Atmos. Chem. Phys.* **2022**, *22* (7), 4355-4374. DOI: 10.5194/acp-22-4355-2022.
(67) Schiferl, L. D.; Heald, C. L.; Nowak, J. B.; Holloway, J. S.; Neuman, J. A.; Bahreini, R.; Pollack, I. B.; Ryerson, T. B.; Wiedinmyer, C.; Murphy, J. G. An investigation of ammonia and inorganic particulate matter in California during the CalNex campaign. *Journal of Geophysical Research: Atmospheres* **2014**, *119* (4), 1883-1902. DOI: https://doi.org/10.1002/2013JD020765.
(68) Van Damme, M.; Clarisse, L.; Franco, B.; Sutton, M. A.; Erisman, J. W.; Wichink Kruit, R.; van Zanten, M.; Whitburn, S.; Hadji-Lazaro, J.; Hurtmans, D.; et al. Global, regional and national trends of atmospheric ammonia derived from a decadal (2008–2018) satellite record. *Environ. Res. Lett.* **2021**, *16* (5), 055017. DOI: 10.1088/1748-9326/abd5e0.
(69) Van Damme, M.; Clarisse, L.; Heald, C. L.; Hurtmans, D.; Ngadi, Y.; Clerbaux, C.; Dolman, A. J.; Erisman, J. W.; Coheur, P. F. Global distributions, time series and error characterization of atmospheric ammonia (NH₃) from IASI satellite observations. *Atmos. Chem. Phys.* **2014**, *14* (6), 2905-2922. DOI: 10.5194/acp-14-2905-2014.
(70) Paulot, F.; Jacob, D. J.; Pinder, R. W.; Bash, J. O.; Travis, K.; Henze, D. K. Ammonia emissions in the United States, European Union, and China derived by high-resolution inversion of ammonium wet deposition data: Interpretation with a new agricultural emissions inventory (MASAGE_NH3). *Journal of Geophysical Research: Atmospheres* **2014**, *119* (7), 4343-4364. DOI: https://doi.org/10.1002/2013JD021130.
(71) Cooper, M. J.; Martin, R. V.; Henze, D. K.; Jones, D. B. A. Effects of a priori profile shape assumptions on comparisons between satellite NO2 columns and model simulations. *Atmos. Chem. Phys.* **2020**, *20* (12), 7231-7241. DOI: 10.5194/acp-20-7231-2020.
(72) Shah, V.; Jacob, D. J.; Dang, R.; Lamsal, L. N.; Strode, S. A.; Steenrod, S. D.; Boersma, K. F.; Eastham, S. D.; Fritz, T. M.; Thompson, C.; et al. Nitrogen oxides in the free troposphere: implications for tropospheric oxidants and the interpretation of satellite NO2 measurements. *Atmos. Chem. Phys.* **2023**, *23* (2), 1227-1257. DOI: 10.5194/acp-23-1227-2023.
(73) Silvern, R. F.; Jacob, D. J.; Mickley, L. J.; Sulprizio, M. P.; Travis, K. R.; Marais, E. A.; Cohen, R. C.; Laughner, J. L.; Choi, S.; Joiner, J.; et al. Using satellite observations of tropospheric NO2 columns to infer long-term trends in US NOx emissions: the importance of accounting for the free tropospheric NO2 background. *Atmos. Chem. Phys.* **2019**, *19* (13), 8863-8878. DOI: 10.5194/acp-19-8863-2019.
(74) Luo, Z.; Zhang, Y.; Chen, W.; Van Damme, M.; Coheur, P. F.; Clarisse, L. Estimating global ammonia (NH3) emissions based on IASI observations from 2008 to 2018. *Atmos. Chem. Phys.* **2022**, *22* (15), 10375-10388. DOI: 10.5194/acp-22-10375-2022.

(75) Ren, C.; Huang, X.; Wang, Z.; Sun, P.; Chi, X.; Ma, Y.; Zhou, D.; Huang, J.; Xie, Y.; Gao, J.; et al. Nonlinear response of nitrate to NOx reduction in China during the COVID-19 pandemic. *Atmos. Environ.* **2021**, *264*, 118715. DOI: https://doi.org/10.1016/j.atmosenv.2021.118715.

(76) Balamurugan, V.; Chen, J.; Qu, Z.; Bi, X.; Keutsch, F. N. Secondary PM2.5 decreases significantly less than NO2 emission reductions during COVID lockdown in Germany. *Atmos. Chem. Phys.* **2022**, *22* (11), 7105-7129. DOI: 10.5194/acp-22-7105-2022.

(77) Yang, S.; Yuan, B.; Peng, Y.; Huang, S.; Chen, W.; Hu, W.; Pei, C.; Zhou, J.; Parrish, D. D.; Wang, W.; et al. The formation and mitigation of nitrate pollution: comparison between urban and suburban environments. *Atmos. Chem. Phys.* **2022**, *22* (7), 4539-4556. DOI: 10.5194/acp-22-4539-2022.

(78) Wen, L.; Xue, L.; Wang, X.; Xu, C.; Chen, T.; Yang, L.; Wang, T.; Zhang, Q.; Wang, W. Summertime fine particulate nitrate pollution in the North China Plain: increasing trends, formation mechanisms and implications for control policy. *Atmos. Chem. Phys.* **2018**, *18* (15), 11261-11275. DOI: 10.5194/acp-18-11261-2018.

(79) Zheng, M.; Wang, Y.; Bao, J.; Yuan, L.; Zheng, H.; Yan, Y.; Liu, D.; Xie, M.; Kong, S. Initial Cost Barrier of Ammonia Control in Central China. *Geophys. Res. Lett.* **2019**, *46* (23), 14175-14184. DOI: https://doi.org/10.1029/2019GL084351.

(80) Paglione, M.; Decesari, S.; Rinaldi, M.; Tarozzi, L.; Manarini, F.; Gilardoni, S.; Facchini, M. C.; Fuzzi, S.; Bacco, D.; Trentini, A.; et al. Historical Changes in Seasonal Aerosol Acidity in the Po Valley (Italy) as Inferred from Fog Water and Aerosol Measurements. *Environ. Sci. Technol.* **2021**, *55* (11), 7307-7315. DOI: 10.1021/acs.est.1c00651.

(81) Petit, J. E.; Dupont, J. C.; Favez, O.; Gros, V.; Zhang, Y.; Sciare, J.; Simon, L.; Truong, F.; Bonnaire, N.; Amodeo, T.; et al. Response of atmospheric composition to COVID-19 lockdown measures during spring in the Paris region (France). *Atmos. Chem. Phys.* **2021**, *21* (22), 17167-17183. DOI: 10.5194/acp-21-17167-2021.

(82) Pusede, S. E.; Duffey, K. C.; Shusterman, A. A.; Saleh, A.; Laughner, J. L.; Wooldridge, P. J.; Zhang, Q.; Parworth, C. L.; Kim, H.; Capps, S. L.; et al. On the effectiveness of nitrogen oxide reductions as a control over ammonium nitrate aerosol. *Atmos. Chem. Phys.* **2016**, *16* (4), 2575-2596. DOI: 10.5194/acp-16-2575-2016.

(83) Kelly, J. T.; Parworth, C. L.; Zhang, Q.; Miller, D. J.; Sun, K.; Zondlo, M. A.; Baker, K. R.; Wisthaler, A.; Nowak, J. B.; Pusede, S. E.; et al. Modeling NH4NO3 Over the San Joaquin Valley During the 2013 DISCOVER-AQ Campaign. *Journal of Geophysical Research: Atmospheres* **2018**, *123* (9), 4727-4745. DOI: https://doi.org/10.1029/2018JD028290.

(84) Prabhakar, G.; Parworth, C. L.; Zhang, X.; Kim, H.; Young, D. E.; Beyersdorf, A. J.; Ziemba, L. D.; Nowak, J. B.; Bertram, T. H.; Faloona, I. C.; et al. Observational assessment of the role of nocturnal residual-layer chemistry in determining daytime surface particulate nitrate concentrations. *Atmos. Chem. Phys.* **2017**, *17* (23), 14747-14770. DOI: 10.5194/acp-17-14747-2017.

(85) Zhai, T.; Lu, K.; Wang, H.; Lou, S.; Chen, X.; Hu, R.; Zhang, Y. Elucidate the formation mechanism of particulate nitrate based on direct radical observations in the Yangtze River Delta summer 2019. *Atmos. Chem. Phys.* **2023**, *23* (4), 2379-2391. DOI: 10.5194/acp-23-2379-2023.

(86) Tan, Z.; Wang, H.; Lu, K.; Dong, H.; Liu, Y.; Zeng, L.; Hu, M.; Zhang, Y. An Observational Based Modeling of the Surface Layer Particulate Nitrate in the North China Plain During Summertime. *Journal of Geophysical Research: Atmospheres* **2021**, *126* (18), e2021JD035623, https://doi.org/10.1029/2021JD035623. DOI: https://doi.org/10.1029/2021JD035623 (acccessed 2023/05/25).

(87) Yang, Y.; Zhao, Y.; Zhang, L.; Zhang, J.; Huang, X.; Zhao, X.; Zhang, Y.; Xi, M.; Lu, Y. Improvement of the satellite-derived NOx emissions on air quality modeling and its effect on ozone and secondary inorganic aerosol formation in the Yangtze River Delta, China. *Atmos. Chem. Phys.* **2021**, *21* (2), 1191-1209. DOI: 10.5194/acp-21-1191-2021.

(88) Lin, Y. C.; Zhang, Y. L.; Fan, M. Y.; Bao, M. Heterogeneous formation of particulate nitrate under ammonium-rich regimes during the high-PM2.5 events in Nanjing, China. *Atmos. Chem. Phys.* **2020**, *20* (6), 3999-4011. DOI: 10.5194/acp-20-3999-2020.

(89) Schmit, T. J.; Li, Z.; Gunshor, M. M.; Iturbide-Iturbide, F.; Yoe, J. G.; McCorkel, J.; Heidinger, A. U.S. Plans for Geostationary Hyperspectral Infrared Sounders. In *IGARSS 2022 - 2022 IEEE International Geoscience and Remote Sensing Symposium*, 17-22 July 2022, 2022; pp 5411-5414. DOI: 10.1109/IGARSS46834.2022.9884082.

(90) Coheur, P.-F.; Levelt, P.; Clarisse, L.; van Damme, M.; Eskes, H.; Veefkind, J. P.; Clerbaux, C.; Dentener, F. J.; Erisman, J. W.; Schaap, M.; et al. Nitrosat, a satellite mission concept for mapping reactive nitrogen at the landscape scale. In EGU General Assembly 2021, online; 2021.